*inorganics*

MDPI

*Article*

# Interplay between Fe-Titanate Nanotube Fragmentation and Catalytic Decomposition of $C_2H_4$: Formation of $C/TiO_2$ Hybrid Interfaces

Federico Cesano [1,*] , Sara Cravanzola [1,*], Mohammed Mastabur Rahman [1,2] and Domenica Scarano [1]

[1]   Department of Chemistry, NIS (Nanostructured Interfaces and Surfaces) Interdepartmental Centre and INSTM Centro di Riferimento, University of Torino, Via P. Giuria, 7, 10125 Torino, Italy; mrahman-cep@sust.edu (M.M.R.); domenica.scarano@unito.it (D.S.)
[2]   Department of Chemical Engineering and Polymer Science, Shahjalal University of Science and Technology (SUST), 3114 Sylhet, Bangladesh
*   Correspondence: federico.cesano@unito.it (F.C.); sara.cravanzola@unito.it (S.C.); Tel.: +39-011-670-7834 (F.C. & S.C.)

check for updates

**Abstract:** This paper reports the synthesis of Fe-titanate nanotubes by means of the conventional ion-exchange method with iron nitrate solutions. As the iron-rich nanotubes were found to contain the catalyst precursor intrinsically dispersed in their structures, the unprecedented possibility of using this kind of materials for building carbon nanostructures, firmly attached at the surface of the forming $TiO_2$ nanoparticles, was verified. The catalytic decomposition of ethylene, used as a carbon source, was performed at a relatively high temperature (750 °C) when the nanotubes undergo an irreversible phase transformation to form anatase and rutile nanoparticles. Due to the different amounts of Fe ions in the nanotubes, distinct types of carbon/$TiO_2$ hybrid interfaces were formed, ranging from amorphous (lower $Fe^{3+}$ concentration) to the more crystalline graphitic domains (higher $Fe^{3+}$ concentrations), as documented by the microstructure of the treated samples. The present approach is of potential interest for (photo)catalytic and energy conversion/transport applications.

## 1. Introduction

The families of one-dimensional (1D) and two-dimensional (2D) nanomaterials have grown noticeably since the discoveries of carbon nanotubes (1991) and of graphene (2004). These 1D/2D nanostructures have opened new perspectives due to their unique properties, which are very different from that of the three-dimensional counterpart [1,2] and to the fact that such nanostructures can be assembled to form composites, hybrids, and van der Waals heterostructures [3–7]. The possibility of building or assembling carbon allotropes and carbon analogues at the surface of another inorganic system, like $TiO_2$ [8–12], provides the opportunity for building interfaces, matching phases with different properties, thus creating domains with predetermined characteristics, but exhibiting new functionalities.

On the other hand, a plethora of opportunities is also available when layered titanates (2D) and/or titanate nanotubes (1D) are taken into consideration [3,13,14]. The formation of anatase nanotubes, obtained from the hydrothermal reaction of $TiO_2$ nanoparticles and NaOH, was initially described by Kasuga et al. [15,16]. Through systematic structural analyses of samples, before and after HCl washing, subsequent studies suggested different structures for the hydrothermally formed nanotubes, including:

$H_2Ti_3O_7$ [17], $H_2Ti_4O_9 \cdot xH_2O$ [18], $H_2Ti_2O_4(OH)_2$ nanotubes [19], and today the consensus of opinion is that the fabricated nanotubes are made of layered titanate or lepidocrocite-type ($H_xTi_{2-x/4}\square_{x/4}O_4 \cdot H_2O$, where $\square$ indicates a vacancy) structures. Both titanate nanotubes, trititanate and lepidocrocite-type, have multilayered structures with walls separated by 0.7–0.8 nm, where $H^+$ are located and can be exchanged with cations [20]. The trititanate nanotubes are composed of steps of corrugated layers, while the lepidocrocite-type is made of a more regular and flat surface, consisting of a continuous and planar 2D array [20]. The reason for investigating these $TiO_2$-based tubular structures comes from their physical and chemical properties which area combination of the distinctive characteristics of the more conventional $TiO_2$ particles (i.e., wide-bandgap, semiconductor-type character) with those of layered titanates (i.e., ion-exchange, proton conductivity) and/or of nanotubes (i.e., small tubular cavities, high surface area and porosity properties).

Hence, such materials have a variety of properties and make these nanomaterials promising for a large variety of applications [20,21]. In particular, catalysis [22], photocatalysis [23], electrochemistry (i.e., anode materials for high-power lithium-ion battery and water splitting) [24], confinement of molecules and nanomedicine [20,21,25] are documented in the literature for titanate nanotubes (TNTs).

The ion-exchange property of TNTs offers another prospect, that is, the opportunity to substitute counterions ($Na^+$, $H^+$, etc.) with other cations, including alkaline ions ($Li^+$, $Na^+$, $K^+$, $Rb^+$, $Cs^+$) [20], transition ($Co^{2+}$, $Ni^{2+}$, $Fe^{3+}$, $Cu^{2+}$, $Zn^{2+}$, $Cd^{2+}$) [20,26,27] and noble metals (Au, Pt, Pd, Ru, Ag) [28,29]. Along with the iron titanate nanotubes, the literature is moderately limited [9,21,26,27,30–38]. Attention has been focused on the electrochemistry [32,38], photocatalysis [31,33,36,37], molecular segregation [27], optical and magnetic properties [21,26,27,31,33] of Fe-titanates. Notwithstanding research and development efforts into the properties of Fe-titanate nanotubes, including the intrinsic ability of iron when present in titanate nanotubes in building carbon domains via catalytic decomposition from light carbon feedstocks, have not been widely explored so far.

In this work, Fe-titanate nanotubes were used as a support to decompose a carbon source (ethylene) at the surface of anatase and rutile nanoparticles under formation, where Fe is expected to play a role as a catalyst. Moreover, by controlling the catalyst content, when the nucleation of larger catalyst particles is promoted, curved graphitic domains are formed. This approach presents the unprecedented possibility of building carbon systems, from amorphous patches to more graphitic domains, firmly attached at the surface of $TiO_2$.

## 2. Results and Discussion

### 2.1. UV–Vis and FTIR Spectroscopies of Fe (III)-Exchanged Titanate Nanotubes

UV–Vis spectroscopy is a fundamental technique for the characterization of transition-metal ions that allows distinguishing highly dispersed cations on/in a solid matrix from more isolated species. Spectral features (intensity, position and shape of bands) can reveal the nature (i.e., symmetry, oxidation state) and the aggregation state of metal ions. Along with the oxidation and coordination states, accurate details are usually given for the d–d transition bands. Such transitions can be assumed as fingerprints for cations having a well-defined oxidation state in the tetrahedral and octahedral coordination, according to Ligand Field Theory (i.e., transitions of $e^-$ within orbitals placed on a central ion). Unfortunately, for Fe cations the explanation is not straightforward due to the fact that: (i) iron in the $d^5$ configuration ($Fe^{3+}$) has very weak transitions (forbidden by the Laporte rule); (ii) ligand-to-metal CT transitions in the tetrahedral and octahedral coordination give bands with similar positions, as documented in the controversial literature on this matter. However, the degree of clustering of Fe cations may be semi-empirically estimated from the UV–Vis features, as the bands are red shifted by increasing the degree of nuclearity [39]. The literature on this subject is well documented by studies on Fe–zeolites (e.g., ZSM-5, beta structures), in which the evolution of Fe species in the UV–Vis spectra, from the more isolated to polynuclear and oxide, is shown [39].

In this context, diffuse reflectance (DR) UV–Vis spectroscopy is adopted here to investigate the nature of the Fe cations on/in titanate nanotubes (HTITs) by using different precursor concentrations (0.001 M, 0.0025 M and 0.01 M). Figure 1 shows the DR UV–Vis spectra obtained on the HTITs before and after ion-exchange in ethanol and the subsequent filtering and drying steps.
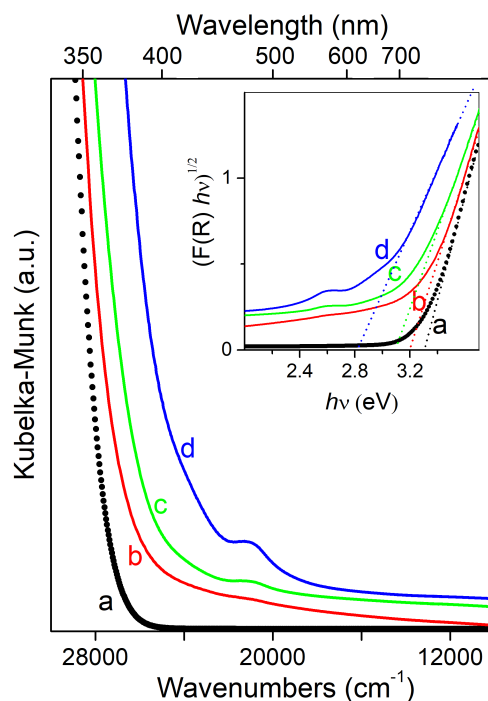


**Figure 1.** Diffuse reflectance UV–Vis spectra of: (a) hydrogen titanate nanotubes and the same nanotubes after ion exchange from $Fe(NO_3)_3$ solutions; (b) 0.001 M; (c) 0.0025 M and (d) 0.01 M. In the inset the relationship between $(F(R)\, h\nu)^{1/2}$ and the photon energy is illustrated.

The spectrum of hydrogen titanate nanotubes (spectrum a), is composed of a strong absorption edge located at ~28,000 $cm^{-1}$ (~357 nm), becoming dominated by the more complex envelope of absorptions in the 28,000–10,000 $cm^{-1}$ range at the increasing concentrations of the $Fe(NO_3)_3$ solutions (b, c and d spectra). More precisely, the spectra are constituted by a first strong absorption extending up to ~25,000 $cm^{-1}$ (400 nm), with a weak shoulder at about 24,000 $cm^{-1}$ (417 nm), an absorption band centered at ~21,000 $cm^{-1}$ and a wider tail up to 10,000 $cm^{-1}$ (1000 nm). All these spectral features, ascribed to nucleation centers (i.e., formation of larger aggregates), develop at the increasing Fe (III) solution concentrations. Hence, the formation of oxide species (those at lower energy) and polymeric Fe species (band at ~21,000 $cm^{-1}$) is inferred. Other features at lower energy can be plausibly ascribed to dinuclear Fe (III) species (28,000–29,000 $cm^{-1}$) and more isolated Fe cations (tetrahedral coordination), but a more detailed description of Fe species is very difficult here due to the presence of the absorption edge of the titanate nanotubes obscuring the 46,000–33,000 $cm^{-1}$ range, where ligand-to-metal CT transitions of Fe (III) in the octahedral coordination with oxygens, are found [40].

In the inset of Figure 1, $(\alpha h\nu)^{1/2}$ is plotted versus the energy for the indirect transitions as obtained by the Tauc plot relation (Tauc and Davis–Mott model):

$$(h\nu\, \alpha)^{1/n} = A(h\nu - E_g)$$

where $h$ is the Planck's constant, $\nu$ is the wavenumber, $\alpha$ = absorption coefficient, A is a constant and $E_g$ is the optical band gap (in eV) for direct ($n = \frac{1}{2}$) or indirect ($n = 2$) transitions, respectively. By assuming F(R) is proportional to the absorption coefficient $\alpha$, it is clearly shown in this plot that the incorporation of iron into the structure of the nanotube alters its lattice and electronic structure.

In more detail, by extrapolating the linear portion of the $(F(R) \times h\nu)^{1/2}$ curves vs. the photon energy $h\nu$, the reduction in the energy bandgap from hydrogen titanate nanotubes (3.3 eV) is well illustrated for the Fe-titanate sample series. By increasing the $Fe^{3+}$ content the value of the bandgap energy progressively decreases from 3.2 eV (curve b: sample ion-exchanged with 0.001 M $Fe(NO_3)_3$ solution) to 3.1 eV and 2.8 eV (curve c and curve d: samples ion-exchanged with 0.0025 M and 0.01 M solutions of $Fe^{3+}$). The decrease in the energy bandgap may be ascribed to the progressive doping iron ions that can form dopant levels near the valence band of the titanate nanotubes.

In conclusion, the UV–Vis spectra of our Fe-TIT samples are similar to those shown for the iron-silicalite, zeolitic structures and mesoporous frameworks [39].

FTIR spectra of the hydrogen titanate nanotubes and of the Fe-TITs#0.01 (exchanged with 0.01 M $Fe^{3+}$) are shown in Figure 2.
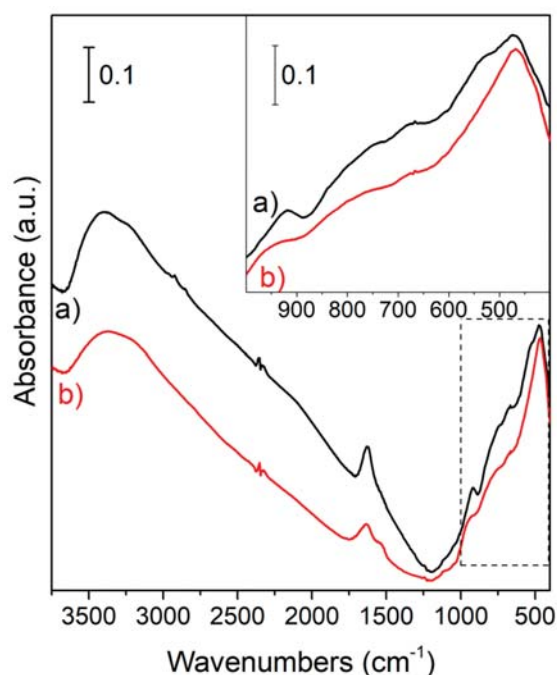


**Figure 2.** FTIR spectra of hydrogen titanate nanotubes (a) before and (b) after ion-exchange with $Fe(NO_3)_3$ 0.01M solution (Fe-TIT#01). In the inset, the two spectra are shown and compared in the 1000–400 $cm^{-1}$ range.

In Figure 2, the bands in the 3600–3000 $cm^{-1}$ and 1690–1550 $cm^{-1}$ intervals (spectrum a) are assigned to stretching and bending vibrations of the –OH groups, respectively, interacting through hydrogen bonds, while those in the 1000–400 $cm^{-1}$ region (inset of Figure 2) are assigned to Ti–O surface and Ti–O–Ti broad phonon bands due to TO vibrational modes [41]. Additionally, the intense band centered at 490 $cm^{-1}$ can be attributed to Ti–O–Ti skeletal modes of the interconnected octahedra forming the TNT walls [41]. In the Fe-titanate sample (spectrum b) an additional peak at about 950 $cm^{-1}$ can be attributed to the Fe–O stretching mode. However, the general erosion of the wide absorption observed in the 880–550 $cm^{-1}$ interval can be explained with the Fe-doping that causes interruptions of the Ti–O–Ti bond linkage [27].

*2.2. Morphology, Structure and Chemical Composition of Fe-Titanate Nanotubes*

The chemical composition, morphology and structure of the hydrogen titanate nanotubes were investigated before and after the ion-exchange with the $Fe(NO_3)_3$ solutions. The results are reported in Figure 3.

The prepared hydrogen titanate nanotubes are constituted by well-shaped and elongated nanostructures 7–10 nm in diameter and several hundred nanometers in length with an internal cavity (Figure 3a). The nanotubes have a multiwalled structure with walls ~7.5 Å spaced, which are parallel to the axis of the nanotube. A second family of fringes ~3.5 Å spaced can be observed at about 74° (Figure 3b). The observed crystal features are in agreement with a lepidocrocite-type titanate structure. The Fe-TIT sample (exchanged with 0.0025 as a molar solution) shows tubular multiwalled nanostructures a few hundred nanometers in length, open-endings, outer and inner diameters of 7–10 nm and of 3–4 nm, respectively (inset of Figure 3c). The walls are ~7.6 Å spaced and the different wall thicknesses, as shown on the different wall sides (Figure 3c), suggest that they are formed through scrolling-up of 1 L sheets, as reported in other studies [13,34]. EDAX spectrum, taken for the Fe-titanate nanotubes shown in Figure 3c, reveals that Fe is present in the structure of the nanotubes (Figure 3d), but no Fe-containing nanoparticles or clusters were imaged by the TEM observations of several nanotubes.
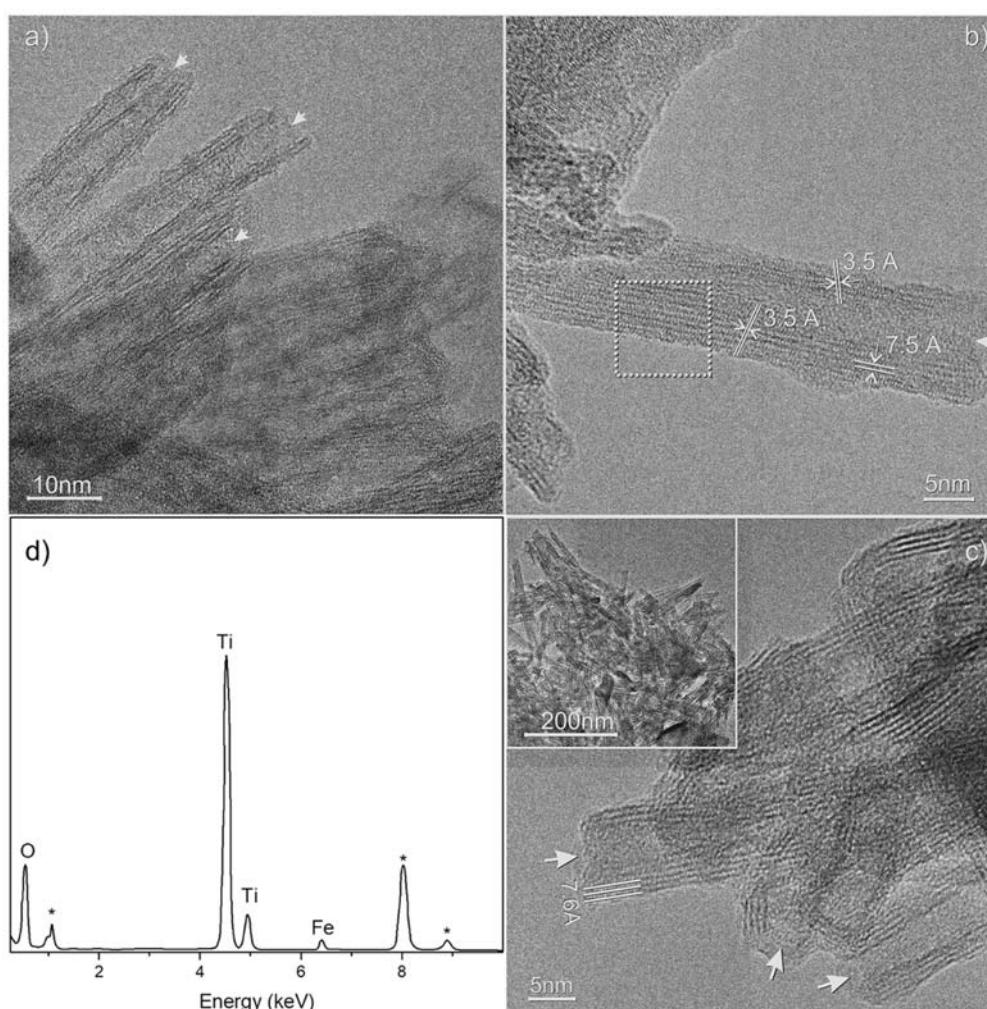


**Figure 3.** HRTEM images of: (**a**,**b**) hydrogen titanate nanotubes; (**c**) the same nanotubes after ion exchange with $Fe(NO_3)_3$ (0.0025 M), and (**d**) the related EDAX spectrum. Cavities of the nanotubes are evidenced by the arrows in **a**–**c**.

This fact is in agreement with the Fe doping in substitutional positions of the lattice [31] observed at low Fe contents, which does not affect the interlayer distance of the walls [20]. Despite the fact that the substitution of $Ti^{4+}$ with $Fe^{3+}$ ions [31,34] or of the hydrated iron complexes of $[Fe_x^{II}(OH)_{2x-1}(OH_2)]^+$ [32], have been shown at low $Fe^{3+}$ concentrations, the presence of isolated

Fe$_x$O$_y$ clusters in our samples escaping from the TEM detection could not be ruled out for the more concentrated Fe-TIT sample, based on the previously discussed UV–Vis spectra.

The Fe contents, as obtained from EDAX spectra of the different Fe-titanate nanotubes, are summarized in Table 1. Although EDAX analysis is only semi-quantitative, it is worth noting that different Fe compositions (~0.4 wt %, 1 wt % and 3 wt %) were found for the Fe-titanate nanotubes ion-exchanged with the different concentrations (0.001 M, 0.0025 M and 0.01 M, respectively) of FeNO$_3$.

**Table 1.** Fe wt % of hydrogen titanate nanotubes after the ion-exchange with Fe(NO$_3$)$_3$ solutions.

| Samples | Molar Concentrations of the Fe(NO$_3$)$_3$ Solutions | Fe wt % |
|---|---|---|
| Fe-TIT#001 | 0.001 | ~0.4 |
| Fe-TIT#0025 | 0.0025 | 1 |
| Fe-TIT#01 | 0.01 | 3 |

### 2.3. Catalytic Decomposition of C$_2$H$_4$ on Fe-Titanate Nanotubes at 750 °C: XRD and TEM Analyses

XRD patterns of Fe-titanate nanotubes, ion-exchanged with different Fe(NO$_3$)$_3$ concentrations (0.001 M, 0.0025M and 0.01M), are reported after thermal decomposition of C$_2$H$_4$ at 750 °C for 1′ (Figure 4).

From this figure, it is clear that the Fe-titanate nanotubes undergo an irreversible phase transformation to form anatase and rutile nanoparticles during the thermal treatments.

More specifically, XRD peaks at 2θ ≈ 25.3°, 36.9°, 37.8°, 48.0°, 53.9°, 55.1° can undoubtedly be assigned to (101), (103), (004), (200), (105) (211) diffraction planes of anatase (PDF card n. #21-1272) and those at 2θ ≈ 27.4°, 36.1°, 39.2°, 41.2°, 44.0°, 54.3° to (110), (101), (200), (112), (210) and (211) diffraction planes of rutile (PDF card n. #21-1276). Besides these remarkable features, minor XRD peaks located at 2θ ≈ 26.4° and at 2θ ≈ 43.0°, 43.7°, 45.0°, 45.9°, 49.0° can be assigned to (002) and at (211), 102), (031), (112), (211) diffraction planes of the hexagonal graphite (data not shown for the sake of brevity) and cementite (PDF card n. #35-0772), respectively. Finally, the XRD peak at 2θ ≈ 44.7° responds to the (110) planes of ferrite (α-Fe, bcc-phased Fe, PDF card n. #06-0696). All these minor features reveal the role played by the Fe catalyst in assembling carbon domains (from amorphous to the more crystalline) via the decomposition of C$_2$H$_4$. Ethylene is known in catalysis not only for the catalytic polymerization/oligomerization [42], but also for the formation of carbon nanostructures, including single-walled carbon nanotubes (SWCNTs) [43], multi-walled carbon nanotubes (MWCNTs) [44], graphene [45], and curved graphitic domains [46].
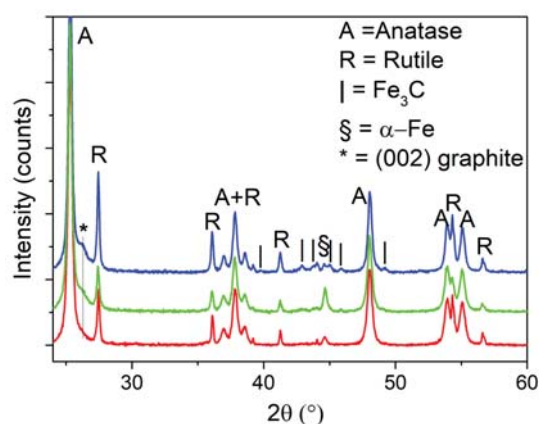


**Figure 4.** XRD patterns after thermal decomposition of C$_2$H$_4$ at 750 °C for 1′ of Fe-titanate nanotubes prepared from different Fe(NO$_3$)$_3$ concentrations: 0.001 M (red curve), 0.0025 M (green curve) and 0.01 M (blue curve). XRD peak positions of anatase (PDF card n. #21-1272), Rutile (PDF card n. #21-1276), cementite: Fe$_3$C (PDF card n. #35-0772), ferrite: α-Fe (bcc-phased Fe, PDF card n. #060696) and of (002) planes of the graphite, are reported for comparison.

To gain more insight into the structure and morphology of samples after being contacted with $C_2H_4$ at 750 °C, TEM images were acquired. The morphological properties of Fe-TITs obtained from the 0.001M solution of $Fe(NO_3)_3$ and treated at 750 °C are shown in Figure 5a.



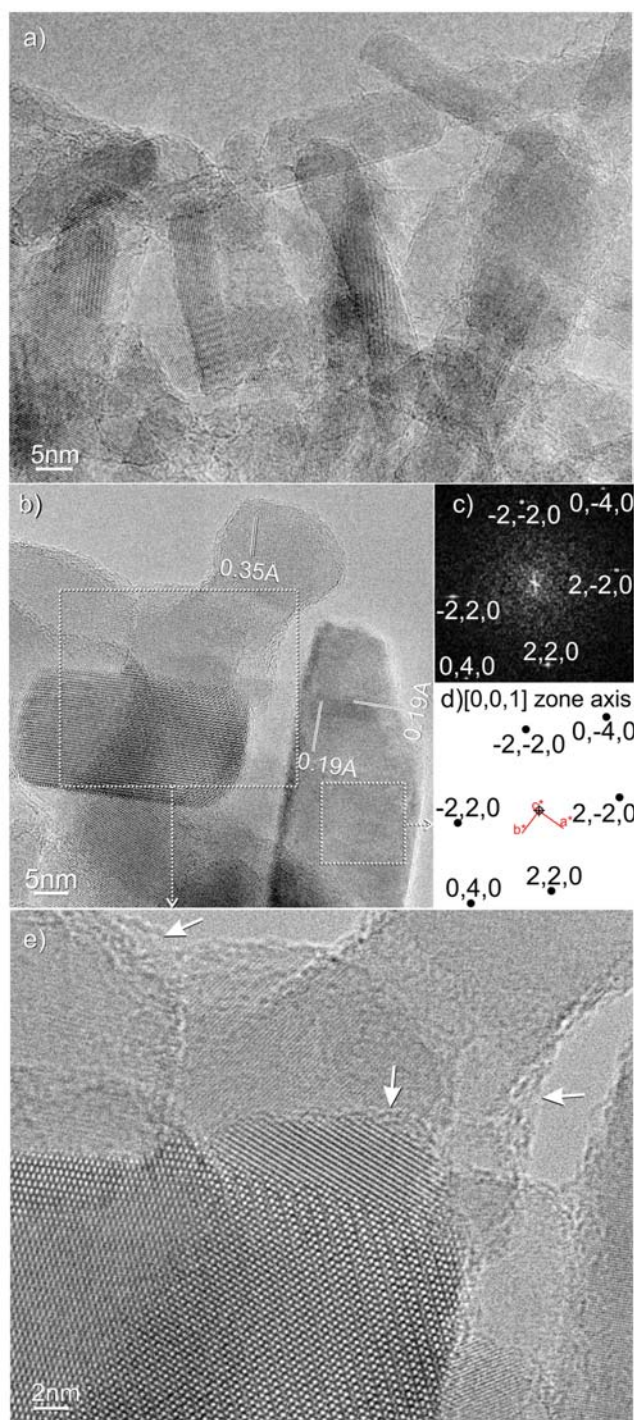**Figure 5.** (**a**,**b**) HRTEM images of Fe-titanate nanotubes (prepared from $Fe(NO_3)_3$ 0.001 M) after thermal decomposition of $C_2H_4$ at 750 °C for 1′; (**c**) experimental FFT image of the nanoparticle selected in (**b**); which is oriented along the [001] zone axis and (**d**) the related simulated SAED pattern of the selected area in (**d**); The arrows in (**e**) highlight the carbon-decorated $TiO_2$ nanoparticle edges.

HRTEM images reveal that elongated (or rod-like) nanoparticles with sizes of 10–30 nm are formed and that such nanocrystals expose fully decorated edges, but nothing more can be inferred at this magnification level. At this point, from a chemical point of view it is important to recall the fact that titanate nanostructures are thermodynamically metastable phases forming $TiO_2$ polymorphs under thermal treatment (with the release of $H_2O$), while from a morphological viewpoint the disappearance of the internal cavity is accompanied by the formation of rod-like nanostructures having a size very close to the external diameter of the initial nanotubes [20,47].

In Figure 5b the amorphous nature of this thin film, covering anatase nanoparticles, is illustrated. Furthermore, an anatase nanocrystal, oriented along the [001] zone axis (see fast-Fourier transform: FFT, and the simulated SAED pattern in Figure 5c,d, respectively), is shown in this figure. Other nanocrystals, exposing fringes 0.35 Å spaced, are associated with (101) planes of anatase.

Finally, the amorphous nature of the thin film at the surface of the nanocrystals is shown (Figure 5e) in a selected region (of Figure 5b).

The situation is completely different if TEM images of Fe-TITs, obtained from the more concentrated solutions of $Fe(NO_3)_3$ (0.0025 M and 0.01 M) are taken into consideration (Figure 6a–d, respectively).
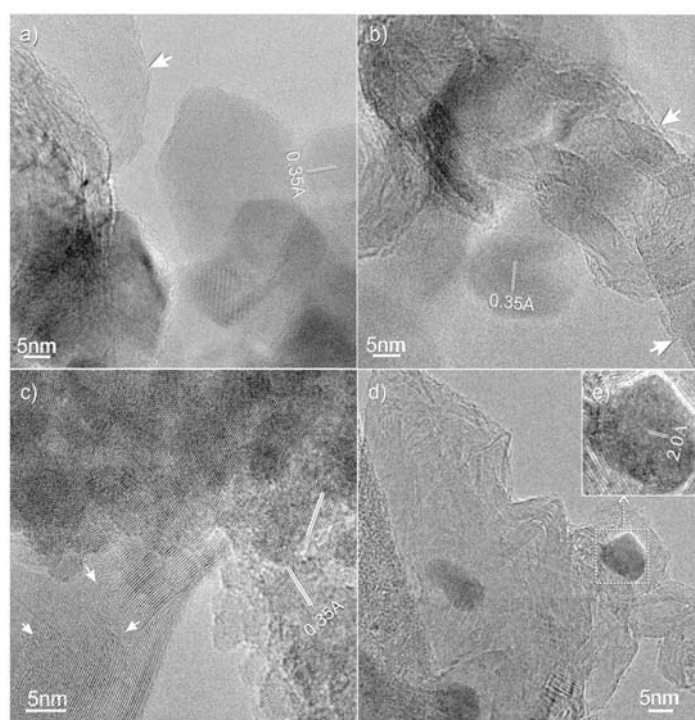


**Figure 6.** HRTEM images of Fe-titanate nanotubes prepared from: (**a**,**b**) 0.0025 M, (**c**,**d**) 0.01 M $Fe(NO_3)_3$ solutions; (**e**) high-resolution image of the region selected in (**d**), after the thermal decomposition of $C_2H_4$ at 750 °C for 1′. The arrows highlight the graphitic domains at the interface with $TiO_2$ nanoparticles (**a**–**c**) and carbon-encapsulated nanoparticles (**d**).

In this figure, the higher crystallinity of carbon (i.e., graphitic stacking) is well documented by regular or more curved structures (see arrows in Figure 6a,c), whose stacking numbers, symmetry and quantities increase with the increase in the amount of nanotube-supported catalyst (higher for titanate nanotubes ion-exchanged with iron nitrate 0.01 M). In the same images, the presence of anatase nanocrystals is evidenced by the regularly 0.35 Å spaced fringes, while the role played by the catalyst in forming graphitic structures is illustrated in Figure 6d, where carbon-encapsulated nanoparticles (see arrows in panel d) have spacing, measured between the adjacent lattice fringes of 2.0 Å, which is in good agreement with the spacing determined from XRD measurements for (110) planes of ferrite (α-Fe).

The yields of carbon have been obtained from the weight loss of the TGA curves for the samples contacted with $C_2H_4$ for 1 min (Figure 7).
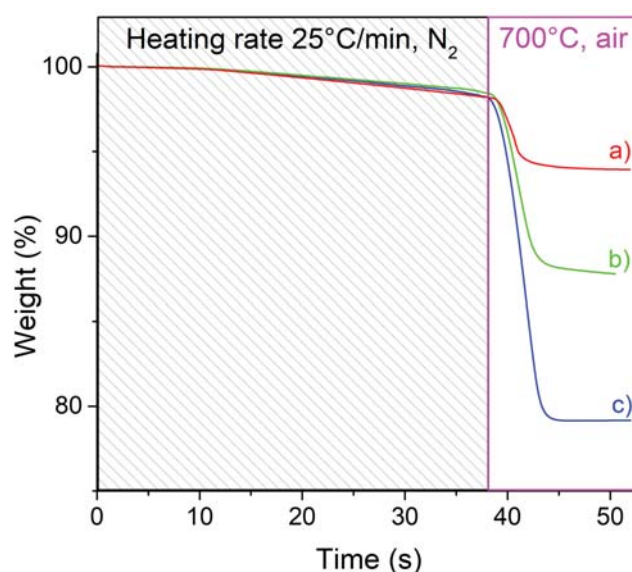


**Figure 7.** TGA curves obtained from a two-step measurement (heating under $N_2$, and oxidation in air at 700 °C) for the Fe-TITs contacted with $C_2H_4$ at 750 °C for 1′: (a) about 0.4 wt %; (b) 2 wt %, and (c) 3 wt % of Fe, respectively.

From this figure, it is clear that the catalyst content (see Table 1) plays a key role in the production of carbons occurring at the surface of the thermally treated Fe-TITs. From a quantitative viewpoint the carbon quantity has been calculated to be ~5 wt %, ~11 wt % and ~21 wt % (for Fe-TITs with about 0.4 wt %, 2 wt % and 3 wt % of Fe, respectively).

These $C/TiO_2$-based hybrid structures show magnetic properties when an external magnet is used more than two years after the preparation (Figure 8 and Supplementary Materials), thus testifying to the good stability to oxidation in air of the encapsulated metal catalyst.

The magnetic character, together with semiconducting properties of $C/TiO_2$, may find application in the photodegradation of pollutants [48,49] due to the easier recovery of the photocatalyst from the solution. Moreover, C-$TiO_2$ interfaces have been shown to be effective in building functional systems for energy conversion applications [50].
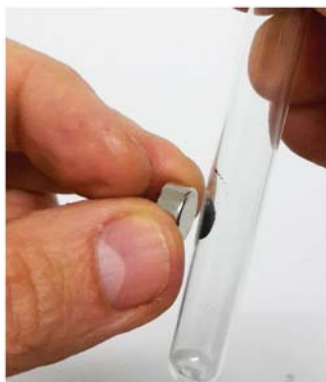


**Figure 8.** Picture showing the macroscopic magnetic properties of $C/TiO_2$ hybrid material coming from the titanate nanotubes ion-exchanged with 0.01 M $Fe(NO_3)_3$ solution and then thermally treated for 1′ at 750 °C with $C_2H_4$.

## 3. Experimental Methods

### 3.1. Synthesis of Materials

Titanate nanotubes were prepared following the procedure described in a previous work [28]. Briefly, $TiO_2$ anatase (Sigma-Aldrich, Milan, Italy) was used as a precursor material and treated with a NaOH solution (10 M) in a PTFE autoclave for 18 h at 150 °C. The as-obtained sodium titanate nanotubes, washed several times by using distilled water and filtered to remove the excess of reactants, were then treated with HCl (0.1 M) for 5 h under stirring. The obtained material was washed, filtered and dried at 120 °C to obtain protonated titanate nanotubes (hereafter H-TITs). Thereafter, H-TITs were treated with $Fe(NO_3)_3 \cdot 9H_2O$ in ethanol solutions (0.001 M, 0.0025 M and 0.01 M) for 20 h. The as-obtained samples (hereafter Fe-TIT) were then filtered with EtOH several times, to remove the excessive $Fe(NO_3)_3$ and dried at 80 °C. Fe-TIT samples were inserted in a quartz tube reactor and thermally treated adopting the following steps: (i) a ramp from RT to 750 °C (heating rate: 15 °C/min) under $N_2$ flow (0.5 L/min); (ii) reaction with a $C_2H_2/H_2$ gas mixture (4:1) at 750 °C for 1 min.

### 3.2. Characterization of Materials

Materials were investigated by UV–Vis spectroscopy (Cary 5000 spectrometer equipped with a reflectance sphere, Varian Inc., Palo Alto, CA, USA), FTIR spectroscopy (Bruker IFS-22 spectrometer having a DTGS detector, Bruker, Billerica, MA, USA), scanning electron microscopy (SEM) (Zeiss Evo 50 instrument equipped with an energy dispersive X-ray (EDAX) detector, Zeiss, Oberkochen, German), transmission electron microscopy (TEM) (3010- UHR instrument operating at 300 kV, JEOL Ltd., Tokyo, Japan), X-ray diffraction (XRD) analysis (PANalytical PW3050/60 X'Pert PRO MPD diffractometer, working with a Ni-filtered Cu anode, Almelo, The Netherland). Zone axis and 3D reciprocal lattices were simulated by means of *CaRIne Crystallography* 3.1 software (Senlis, France). Thermogravimetric analysis (TGA) (Q600, TA instruments, New Castle, USA) was performed in order to quantify the carbon content after the reaction with $C_2H_2$.

## 4. Conclusions

The preparation of Fe-titanate nanotubes from hydrogen titanate and $Fe(NO_3)_3$ solutions by means of the ion-exchange method is reported. As the Fe-rich titanate nanotubes contain the catalyst precursor intrinsically dispersed in their structures, the unprecedented possibility of this kind of system of building carbon nanostructures, firmly attached at the surface of the forming $TiO_2$ nanoparticles was verified. The catalytic decomposition of ethylene, used as a carbon source, was performed at a relatively high temperature (750 °C), at which the titanate nanotubes undergo an irreversible phase transformation into anatase and rutile nanoparticles. Due to the different amounts of Fe ions, different types of carbon/$TiO_2$ hybrid interfaces were obtained, ranging from amorphous (lower $Fe^{3+}$ concentration) to the more crystalline graphitic domains (higher $Fe^{3+}$ concentration), as documented by the microstructure of the treated samples. The present approach is of potential interest for (photo)catalytic and energy conversion/transport applications.

# References

1.  Novoselov, K.S.; Mishchenko, A.; Carvalho, A.; Castro Neto, A.H. 2D materials and Van der waals heterostructures. *Science* **2016**, *353*, aac9439. [CrossRef] [PubMed]
2.  Zhang, Q.; Huang, J.Q.; Qian, W.Z.; Zhang, Y.Y.; Fei Wei, F. The road for nanomaterials industry: A review of carbon nanotube production, post-treatment, and bulk applications for composites and energy storage. *Small* **2013**, *9*, 1237–1265. [CrossRef] [PubMed]
3.  Wang, W.; Wang, Z.; Liu, J.; Zhang, Z.; Sun, L. Single-step one-pot synthesis of graphene foam/$TiO_2$ nanosheet hybrids for effective water treatment. *Sci. Rep.* **2017**, *7*, 43755. [CrossRef] [PubMed]
4.  Cravanzola, S.; Jain, S.M.; Cesano, F.; Damin, A.; Scarano, D. Development of a multifunctional $TiO_2$/MWCNT hybrid composite grafted on a stainless steel grating. *RSC Adv.* **2015**, *5*, 103255–103264. [CrossRef]
5.  Cravanzola, S.; Cesano, F.; Magnacca, G.; Zecchina, A.; Scarano, D. Designing rGO/$MoS_2$ hybrid nanostructures for photocatalytic applications. *RSC Adv.* **2016**, *6*, 59001–59008. [CrossRef]
6.  Bubnova, O. 2D materials: Hybrid interfaces. *Nat. Nanotechnol.* **2016**, *16*, 497–503. [CrossRef]
7.  Badhulika, S.; Terse-Thakoor, T.; Villarreal, C.; Mulchandani, A. Graphene hybrids: Synthesis strategies and applications in sensors and sensitized solar cells. *Front. Chem.* **2015**, *3*, 38. [CrossRef] [PubMed]
8.  Cravanzola, S.; Sarro, M.; Cesano, F.; Calza, P.; Scarano, D. Few-layer $MoS_2$ nanodomains decorating $TiO_2$ nanoparticles: A case study for the photodegradation of carbamazepine. *Nanomaterials* **2018**, *8*, 207. [CrossRef] [PubMed]
9.  Lu, J.; Deng, C.; Zhang, X.; Yang, P. Synthesis of $Fe_3O_4$/graphene/$TiO_2$ composites for the highly selective enrichment of phosphopeptides from biological samples. *ACS Appl. Mater. Interfaces* **2013**, *5*, 7330–7334. [CrossRef] [PubMed]
10. Cravanzola, S.; Cesano, F.; Gaziano, F.; Scarano, D. Carbon domains on $MoS_2$/$TiO_2$ system via acetylene polymerization: Synthesis, structure and surface properties. *Front. Chem.* **2017**, 91. [CrossRef] [PubMed]
11. Cesano, F.; Pellerej, D.; Scarano, D.; Ricchiardi, G.; Zecchina, A. Radially organized pillars of $TiO_2$ nanoparticles: Synthesis, characterization and photocatalytic tests. *J. Photochem. Photobiol. A Chem.* **2012**, *242*, 51–58. [CrossRef]
12. Cesano, F.; Bertarione, S.; Damin, A.; Agostini, G.; Usseglio, S.; Vitillo, J.G.; Lamberti, C.; Spoto, G.; Scarano, D.; Zecchina, A. Oriented $TiO_2$ nanostructured pillar arrays: Synthesis and characterization. *Adv. Mater.* **2008**, *20*, 3342–3348. [CrossRef]
13. Cravanzola, S.; Muscuso, L.; Cesano, F.; Agostini, G.; Damin, A.; Scarano, D.; Zecchina, A. $MoS_2$ nanoparticles decorating titanate-nanotube surfaces: Combined microscopy, spectroscopy and catalytic studies. *Langmuir* **2015**, *31*, 5469–5478. [CrossRef] [PubMed]
14. Yao, Z.; Xia, X.; Zhong, Y.; Wang, Y.; Zhang, B.; Xie, D.; Wang, X.; Tu, J.; Huang, Y. Hybrid vertical graphene/lithium titanate–CNTs arrays for lithium ion storage with extraordinary performance. *J. Mater. Chem. A* **2017**, *5*, 8916–8921. [CrossRef]
15. Kasuga, T.; Hiramatsu, M.; Hoson, A.; Sekino, T.; Niihara, K. Titania nanotubes prepared by chemical processing. *Adv. Mater.* **1999**, *11*, 1307–1311. [CrossRef]
16. Kasuga, T.; Hiramatsu, M.; Hoson, A.; Sekino, T.; Niihara, K. Formation of titanium oxide nanotube. *Langmuir* **1998**, *14*, 3160–3163. [CrossRef]
17. Chen, Q.; Zhou, W.; Du, G.; Peng, L.-M. Trititanate nanotubes made via a single alkali treatment. *Adv. Mater.* **2002**, *14*, 1208–1211. [CrossRef]
18. Nakahira, A.; Kato, W.; Tamai, M.; Isshiki, T.; Nishio, K.; Aritani, H. Synthesis of nanotube from a layered $H_2Ti_4O_9$ $H_2O$ in a hydrothermal treatment using various titania sources. *J. Mater. Sci.* **2004**, *39*, 4239–4245. [CrossRef]
19. Yang, J.; Jin, Z.; Wang, X.; Li, W.; Zhang, J.; Zhang, S.; Guo, X.; Zhang, Z. Study on composition, structure and formation process of nanotube $Na_2Ti_2O_4(OH)_2$. *Dalton Trans.* **2003**, *20*, 3898–3901. [CrossRef]
20. Bavykin, D.V.; Friedrich, J.M.; Walsh, F.C. Protonated titanates and $TiO_2$ nanostructured materials: Synthesis, properties, and applications. *Adv. Mater.* **2006**, *18*, 2807–2824. [CrossRef]
21. Chen, Q.; Peng, L. Structure and applications of titanate and related nanostructures. *Int. J. Nanotechnol.* **2007**, *4*, 44–65. [CrossRef]

22. Khawaji, M.; Chadwick, D. Au-Pd bimetallic nanoparticles immobilised on titanate nanotubes: A highly active catalyst for selective oxidation. *ChemCatChem* **2017**, *9*, 4353–4363. [CrossRef]

23. Nguyen, N.H.; Bai, H. Photocatalytic removal of NO and $NO_2$ using titania nanotubes synthesized by hydrothermal method. *J. Environ. Sci.* **2014**, *26*, 1180–1187. [CrossRef]

24. Zhang, H.; Kim, J.H.; Kim, J.H.; Lee, J.S. Engineering highly ordered iron titanate nanotube array photoanodes for enhanced solar water splitting activity. *Adv. Funct. Mater.* **2017**, *27*, 1702428. [CrossRef]

25. Julien Boudon, J.; Papa, A.L.; Paris, J.; Millot, N. Titanate nanotubes as a versatile platform for nanomedicine. In *Nanomedicine*; Seifalian, A., De Mel, A., Kalaskar, D.M., Eds.; One Central Press: Cheshire, UK, 2014; pp. 405–429.

26. Wang, M.; Song, G.; Li, J.; Miao, L.; Zhang, B. Direct hydrothermal synthesis and magnetic property of titanate nanotubes doped magnetic metal ions. *J. Univ. Sci. Technol. Beijing* **2008**, *15*, 644–648. [CrossRef]

27. Dai, L.; Zheng, J.; Wang, L. Fabrication of titanate nanotubes/iron oxide magnetic composite for the high efficient capture of radionuclides: A case investigation of [109]Cd (II). *J. Radioanal. Nucl. Chem.* **2013**, *298*, 1947–1956. [CrossRef]

28. Cesano, F.; Bertarione, S.; Uddin, M.J.; Agostini, G.; Scarano, D.; Zecchina, A. Designing $TiO_2$ based nanostructures by control of surface morphology of pure and silver loaded titanate nanotubes. *J. Phys. Chem. C* **2010**, *114*, 169–178. [CrossRef]

29. Walsh, F.C.; Bavykin, D.V.; Torrente-Murciano, L.; Lapkin, A.A.; Cressey, B.A. Synthesis of novel composite materials via the deposition of precious metals onto protonated titanate ($TiO_2$) nanotubes. *Trans. Inst. Metal Finish.* **2006**, *86*, 293–299. [CrossRef]

30. Fu, G.; Wei, G.; Yang, Y.; Xiang, W.C.; Qiao, N. Facile synthesis of Fe-doped titanate nanotubes with enhanced photocatalytic activity for castor oil oxidation. *J. Nanomater.* **2013**, *2013*, 1–4. [CrossRef]

31. Han, W.Q.; Wen, W.; Yi, D.; Liu, Z.; Maye, M.M.; Lewis, L.; Hanson, J.; Gang, O. Fe-doped trititanate nanotubes: Formation, optical and magnetic properties, and catalytic applications. *J. Phys. Chem. C* **2007**, *111*, 14339–14342. [CrossRef]

32. Jang, J.S.; Kim, D.H.; Choi, S.H.; Jang, J.W.; Kim, H.G.; Lee, J.S. In-situ synthesis, local structure, photoelectrochemical property of Fe-intercalated titanate nanotube. *Int. J. Hydrog. Energy* **2012**, *37*, 11081–11089. [CrossRef]

33. Morín, M.E.Z.; Torres-Martínez, L.; Sanchez-Martínez, D.; Gómez-Solís, C. Photocatalytic performance of titanates with formula $MTiO_3$ (M = Fe, Ni, and Co) synthesized by solvo-combustion method. *Mater. Res.* **2017**, *20*, 1322–1331. [CrossRef]

34. Pang, Y.L.; Abdullah, Z.A. Effect of low $Fe^{3+}$ doping on characteristics, sonocatalytic activity and reusability of $TiO_2$ nanotubes catalysts for removal of rhodamine b from water. *J. Hazard. Mater.* **2012**, *235–236*, 326–335. [CrossRef] [PubMed]

35. Yu, J.; Xiang, Q.; Zhou, M. Preparation, characterization and visible-light-driven photocatalytic activity of Fe-doped titania nanorods and first-principles study for electronic structures. *Appl. Catal. B Environ.* **2009**, *90*, 595–602. [CrossRef]

36. Zhang, K.Z.; Lin, B.Z.; Chen, Y.L.; Xu, B.H.; Pian, X.T.; Kuang, J.D.; Li, B. Fe-doped and ZnO-pillared titanates as visible-light-driven photocatalysts. *J. Colloid Interface Sci.* **2011**, *358*, 360–368. [CrossRef] [PubMed]

37. Yuan, R.; Zhou, B.; Hua, D.; Shi, C. Effect of metal ion-doping on characteristics and photocatalytic activity of $TiO_2$ nanotubes for removal of humic acid from water. *Front. Environ. Sci. Eng.* **2015**, *9*, 850–860. [CrossRef]

38. Wang, Y.-X.; Xie, J.; Cao, G.-S.; Zhu, T.-J.; Zhao, X.-B. Electrochemical performance of $TiO_2$/carbon nanotubes nanocomposite prepared by an in situ route for Li-ion batteries. *J. Mater. Res.* **2012**, *27*, 417–423. [CrossRef]

39. Čapek, L.; Kreibich, V.; Dědeček, J.; Grygar, T.; Wichterlova, B.; Sobalìk, Z.; Martens, J.A.; Brosius, R.; Tokarová, V. Analysis of Fe species in zeolites by UV–Vis–NIR, IR spectra and voltammetry. Effect of preparation, Fe loading and zeolite type. *Microporous Mesoporous Mater.* **2005**, *80*, 279–289. [CrossRef]

40. Lopez, L.; de Laat, J.; Legube, B. Charge transfer of iron (III) monomeric and oligomeric aqua hydroxo complexes: Semiempirical investigation into photoactivity. *Inorg. Chem.* **2002**, *41*, 2505–2517. [CrossRef]

41. Muniyappan, S.; Solaiyammal, T.; Sudhakar, K.; Karthigeyan, A.; Murugakoothan, P. Conventional hydrothermal synthesis of titanate nanotubes: Systematic discussions on structural, optical, thermal and morphological properties. *Mod. Electron. Mater.* **2017**, *3*, 174–178. [CrossRef]

42. Groppo, E.; Lamberti, C.; Cesano, F.; Zecchina, A. On the fraction of Cr-II sites involved in the $C_2H_4$ polymerization on the $Cr/SIO_2$ Phillips catalyst: A quantification by FTIR spectroscopy. *PCCP* **2006**, *8*, 2453–2456. [CrossRef] [PubMed]

43. Jain, S.M.; Cesano, F.; Scarano, D.; Edvinsson, T. Resonance Raman and IR spectroscopy of aligned carbon nanotube arrays with extremely narrow diameters prepared with molecular catalysts on steel substrates. *PCCP* **2017**, *19*, 30667–30674. [CrossRef] [PubMed]

44. Cesano, F.; Bertarione, S.; Scarano, D.; Zecchina, A. Connecting carbon fibers by means of catalytically grown nanofilaments: Formation of carbon–carbon composites. *Chem. Mater.* **2005**, *17*, 5119–5123. [CrossRef]

45. Cabrero-Vilatela, A.; Weatherup, R.S.; Braeuninger-Weimer, P.; Caneva, S.; Hofmann, S. Towards a general growth model for graphene CVD on transition metal catalysts. *Nanoscale* **2016**, *8*, 2149–2158. [CrossRef] [PubMed]

46. Cesano, F.; Rahman, M.M.; Bardelli, F.; Damin, A.; Scarano, D. Magnetic hybrid carbon via graphitization of polystyrene-*co*-divinylbenzene: Morphology, structure and adsorption properties. *Chem. Select* **2016**, *1*, 2536–2541. [CrossRef]

47. Morgado, E.; de Abreu, M.A.S.; Pravia, O.R.C.; Marinkovic, B.A.; Jardim, P.M.; Rizzo, F.C.; Araújo, A.S. A study on the structure and thermal stability of titanate nanotubes as a function of sodium content. *Solid State Sci.* **2006**, *8*, 888–900. [CrossRef]

48. Cesano, F.; Fenoglio, G.; Carlos, L.; Nisticò, R. One-step synthesis of magnetic chitosan polymer composite films. *Appl. Surf. Sci.* **2015**, *345*, 175–181. [CrossRef]

49. Shrestha, N.K.; Macak, J.M.; Schmidt-Stein, F.; Hahn, R.; Mierke, C.T.; Fabry, B.; Schmuki, P. Magnetically guided titania nanotubes for site-selective photocatalysis and drug release. *Angew. Chem.* **2009**, *121*, 987–990. [CrossRef]

50. Uddin, M.J.; Daramola, D.E.; Velasquez, E.; Dickens, T.J.; Yan, J.; Hammel, E.; Cesano, F.; Okoli, O.I. A high efficiency 3D photovoltaic microwire with carbon nanotubes (CNT)-quantum dot (QD) hybrid interface. *Phys. Status Solidi RRL* **2014**, *8*, 898–903. [CrossRef]